Supplemental Material to "Tracing long-lived atomic coherences generated via molecular conical intersections"

Patrick Rupprecht,[1,2,*] Francesco Montorsi,[3,†] Lei Xu,[4] Nicolette G. Puskar,[1,2] Marco Garavelli,[3] Shaul Mukamel,[5] Niranjan Govind,[4,6] Daniel M. Neumark,[1,2,‡] Daniel Keefer,[7,§] and Stephen R. Leone[1,2,8,¶]

[1]*Department of Chemistry, University of California, Berkeley, California 94720, USA*
[2]*Chemical Sciences Division, Lawrence Berkeley National Laboratory, Berkeley, California 94720, USA*
[3]*Università di Bologna - Alma Mater Studiorum, Via Piero Gobetti 85, 40129 - Bologna, Italy*
[4]*Physical and Computational Sciences Directorate, Pacific Northwest National Laboratory, Richland, WA 99352, USA*
[5]*Department of Chemistry and Department of Physics and Astronomy, University of California, Irvine, California 92697-2025, USA*
[6]*Department of Chemistry, University of Washington, Seattle, WA 98195, USA*
[7]*Max Planck Institute for Polymer Research, Mainz 55128, Germany*
[8]*Department of Physics, University of California, Berkeley, California 94720, USA*

(Dated: October 21, 2025)

I. EFFECTIVE HAMILTONIAN

The photoinduced bond cleavage in methyl iodide and the corresponding four-wave-mixing (FWM) signals are modeled via explicit wave packet propagation (quantum dynamics; QD) on a two-dimensional Hamiltonian $\hat{H}$. The two nuclear degrees of freedom spanning the coordinate system of $\hat{H}$ have been selected to encompass a large cross-section of the ${}^3Q_0/{}^1Q_1$ branching plane. In particular, this space comprises the symmetry preserving C−I stretching (R; *reactive* mode) and the symmetry breaking H−C−I bending (φ; *coupling* mode). Such a Hamiltonian is an adaptation of the full nine-dimensional *ab-initio* model parametrized by Amatatsu *et al.* [1] and further corrected by Xie *et al.* [2]. Five different diabatic states are included in the model, namely: the ground $\tilde{X}(A_1)$ state, the valence excited ${}^3Q_0$ and ${}^1Q_1$ states, and the two spin-orbit-split $\sigma^*(4d_{5/2})^{-1}$ and $\sigma^*(4d_{3/2})^{-1}$ core-excited states. This Hamiltonian reads

$$\hat{H}(t) = \begin{pmatrix} \hat{T} + \hat{V}_{\tilde{X}(A_1)} & -\hat{\boldsymbol{\mu}}_{\tilde{X}^3Q_0} \cdot \mathbf{E}(t) & -\hat{\boldsymbol{\mu}}_{\tilde{X}^1Q_1} \cdot \mathbf{E}(t) & 0 & 0 \\ -\hat{\boldsymbol{\mu}}_{\tilde{X}^3Q_0} \cdot \mathbf{E}(t) & \hat{T} + \hat{V}_{^3Q_0} & \hat{K}_{^3Q_0^1Q_1} & 0 & 0 \\ -\hat{\boldsymbol{\mu}}_{\tilde{X}^1Q_1} \cdot \mathbf{E}(t) & \hat{K}_{^3Q_0^1Q_1} & \hat{T} + \hat{V}_{^1Q_1} & 0 & 0 \\ 0 & 0 & 0 & \hat{T} + \hat{V}_{\sigma^*(4d_{5/2})^{-1}} & 0 \\ 0 & 0 & 0 & 0 & \hat{T} + \hat{V}_{\sigma^*(4d_{3/2})^{-1}} \end{pmatrix}, \tag{S1}$$

where $\hat{T}$ and $\hat{V}$ are kinetic and potential energy operators, respectively, $\hat{K}$ is the diabatic coupling between the valence excited states, $\hat{\boldsymbol{\mu}}$ is the dipole coupling between the ground and the valence excited sates and $\mathbf{E}(t)$ is the electric field of the pump pulse that initiates the dynamics. The dependence upon R and φ is here omitted for simplicity.

I.I. ${}^3Q_0$ and ${}^1Q_1$ potential energy surfaces

The $\hat{V}_{^3Q_0}(R,\varphi)$ and $\hat{V}_{^1Q_1}(R,\varphi)$ potential energy surfaces used in this work are written employing the same notation as used in Ref. [1]. In particular, we use A and B to identify the parameters of $\hat{V}_{^1Q_1}(R,\varphi)$ and $\hat{V}_{^3Q_0}(R,\varphi)$, respectively. Moreover, the superscript $\prime$ is introduced as further distinction between different parameters belonging to the same potential. Following this notation the ${}^1Q_1$ and ${}^3Q_0$ PESs read:

$$\begin{aligned} \hat{V}_{^3Q_0}(R,\varphi) =& \Delta E_I + \Delta E_{CH_3} + (B_0 + B_1\Delta R + B_2\Delta R^2 + B_3')e^{-B_4\Delta R} + \\ &+ [B_7'(\cos(\Delta\varphi) - 1) + B_8(\cos(2\Delta\varphi) - 1) + \\ &+ (B_3' - B_7')(\cos(3\Delta\varphi) - 1) + B_9\sin(\Delta\varphi)]\, e^{-B_4\Delta R} \end{aligned} \tag{S2}$$

$$\begin{aligned} \hat{V}_{^1Q_1}(R,\varphi) =& \Delta E_{CH_3} + (A_0 + A_1\Delta R + A_2\Delta R^2 + A_3')e^{-A_4\Delta R} + \\ &+ [A_7'(\cos(\Delta\varphi) - 1) + A_8(\cos(2\Delta\varphi) - 1) + \\ &+ (A_3' - A_7')(\cos(3\Delta\varphi) - 1) + A_9\sin(\Delta\varphi)]\, e^{-A_4\Delta R} \end{aligned} \tag{S3}$$

where ΔE_I is the energy difference between the ground ($^2P_{3/2}$) and the excited ($^2P_{1/2}$) states of the isolated iodine atom ($\Delta E_I = 0.0343646\,\text{a.u.} = 0.935\,\text{eV}$). This value correspond to the spin-orbit splitting between the two atomic iodine states. ΔR is defined as the displacement of the C−I stretching (R) with respect to its equilibrium position $R_e = 4.04095\,\text{a.u.} = 2.14\,\text{Å}$, i.e. $\Delta R = R - R_e$. Similarly, $\Delta\varphi$ is the displacement along the H−C−I bending (φ) defined with respect to its equilibrium value ($\varphi_e = 108.5°$), i.e. $\Delta\varphi = \varphi - \varphi_e$. ΔE_{CH_3} is the energy gap between the original system and the methyl fragment in its ground state (roughly 2.70 eV). This value has been extracted from electronic structure calculations as the asymptotic limit of the $\tilde{X}(A_1)$ state energy when R approaches infinity.
In the above expressions the A/B coefficients can be represented as a cosine series P_i:

$$P_i = P_{i,0} + P_{i,1}\cos(\Delta\alpha) + P_{i,2}\cos(2\Delta\alpha)\ , \tag{S4}$$

with i running over A/B coefficients. Analogously, the A'/B' coefficients can be represented by the generic L_i parameter which reads:

$$L_i = L_{i,0} + L_{i,1}\sin(\Delta\alpha) + L_{i,2}\sin(2\Delta\alpha)\ , \tag{S5}$$

where $\Delta\alpha$ in our case is the displacement of the H−C−I equilibrium angle (φ_e) with respect to 90° (i.e. $\Delta\alpha = 18.5°$) and the P and L parameters can be taken from Ref. [1]. In particular, the set of L parameter in Ref. [1] is named Q. Here, we have decided to modify such nomenclature to prevent any potential conflict with $^3Q_0$ and $^1Q_1$ labeling of the CH_3I excited states.
The diabatic coupling element $\hat{K}_{^3Q_0^1Q_1}(R,\varphi)$ is defined as:

$$\hat{K}_{^3Q_0^1Q_1}(R,\varphi) = \frac{D_1\sin(\Delta\varphi) + D_2'\sin(2\Delta\varphi)}{(R-D_3)^2 + D_4^2}\quad , \tag{S6}$$

where the coefficients D and D' are also given in the form of Eqs. (S4) and (S5), respectively, with adapted P an Q coefficients given in Ref. [1]. The diabatic $^3Q_0$ and $^1Q_1$ PESs as well as their diabatic coupling are shown in Fig. S1.

I.II. $\tilde{X}(A_1)$, $\sigma^*(4d_{5/2})^{-1}$ and $\sigma^*(4d_{3/2})^{-1}$ potential energy surfaces

The model parametrized by Amatatsu *et al.* [1] does not provide an expression for the $\tilde{X}(A_1)$, $\sigma^*(4d_{5/2})^{-1}$ and $\sigma^*(4d_{3/2})^{-1}$ potential energy surfaces. Therefore, MRCI calculations were performed to evaluate the energies of these electronic states on a spatial grid spanned by the R and φ degrees of freedom. However, 12 adiabatic spin-orbit states of $\sigma^*(4d_{5/2})^{-1}$ and 8 of $\sigma^*(4d_{3/2})^{-1}$ nature were identified from MRCI calculations [see Fig. S4(a)]. In order to reduce the computational effort required to evaluate the FWM signal we define two mean $\sigma^*(4d_{5/2})^{-1}$ and $\sigma^*(4d_{3/2})^{-1}$ states characterized by the average energy and cumulative transition dipole moments with other states (i.e. defined as the sum of transition dipole moment magnitudes). Such an approximation is enabled by the almost negligible energy splitting between states of the same branch, which makes such a fine structure impossible to be detected in the proposed experiment.
The results of these electronic structure calculations are then used to fit analytical expressions for the three potentials. In particular, we rely on the same functional form employed in Eqs. (S2) and (S3), which results in the following expressions:

$$\begin{aligned}\hat{V}_{\tilde{X}(A_1)}(R,\varphi) =& \Delta E_{CH_3} + (k_0^\alpha + k_1^\alpha\Delta R + k_2^\alpha\Delta R^2 + k_3^\alpha)e^{-k_4^\alpha\Delta R} + \\ &+ [k_5^\alpha(\cos\Delta\varphi - 1) + k_6^\alpha(\cos(2\Delta\varphi) - 1) + \\ &+ (k_3^\alpha - k_5^\alpha)(\cos(3\Delta\varphi) - 1) + k_7^\alpha\sin\Delta\varphi]\, e^{-k_4^\alpha\Delta R}\end{aligned} \tag{S7}$$

$$\begin{aligned}\hat{V}_{\sigma^*(4d_{5/2})^{-1}}(R,\varphi) =& \Delta E_{(4d_{5/2})^{-1}} + \Delta E_{CH_3} + (k_0^\beta + k_1^\beta\Delta R + k_2^\beta\Delta R^2 + k_3^\beta)e^{-k_4^\beta\Delta R} + \\ &+ \Big[k_5^\beta(\cos\Delta\varphi - 1) + k_6^\beta(\cos(2\Delta\varphi) - 1) + \\ &+ (k_3^\beta - k_5^\beta)(\cos(3\Delta\varphi) - 1) + k_7^\beta\sin\Delta\varphi\Big]\, e^{-k_4^\beta\Delta R}\end{aligned} \tag{S8}$$

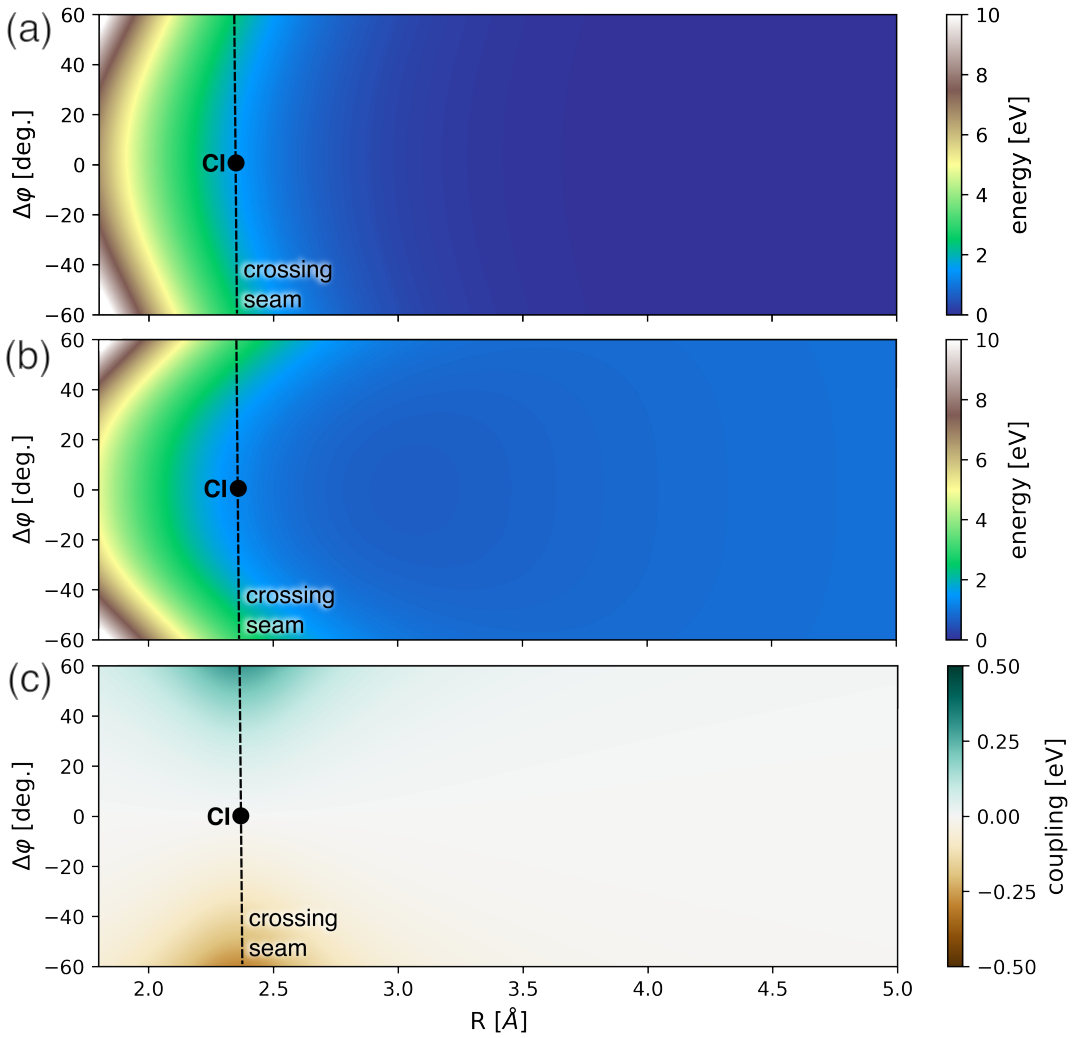

FIG. S1: PESs of the $^1Q_1$ (a) and $^3Q_0$ (b) states, respectively. Here, the $E = 0$ energy is determined by the atomic iodine ground state energy. This is achieved by subtracting $\Delta E_{\mathrm{CH_3}}$ from both Eq. (S3) and Eq. (S2). (c) Diabatic coupling between $^1Q_1$ and $^3Q_0$ states. The crossing seam and the position of the molecular CI are highlighted by black dashed lines and black dots, respectively.

TABLE S1: Energy gap extracted from MRCI calculations.

ΔE_{CH_3}	$\Delta E_{(4d_{5/2})^{-1}}$	$\Delta E_{(4d_{3/2})^{-1}}$
0.09928 a.u. (2.70 eV)	1.70424 a.u. (46.37 eV)	1.76545 a.u. (48.04 eV)

$$\begin{aligned}\hat{V}_{\sigma^*(4d_{3/2})^{-1}}(R,\varphi) =& \Delta E_{(4d_{3/2})^{-1}} + \Delta E_{CH_3} + (k_0^\gamma + k_1^\gamma \Delta R + k_2^\gamma \Delta R^2 + k_3^\gamma) e^{-k_4^\gamma \Delta R} + \\ &+ [k_5^\gamma(\cos\Delta\varphi - 1) + k_6^\gamma(\cos(2\Delta\varphi) - 1) + \\ &+ (k_3^\gamma - k_5^\gamma)(\cos(3\Delta\varphi) - 1) + k_7^\gamma \sin\Delta\varphi]\, e^{-k_4^\gamma \Delta R}\end{aligned} \tag{S9}$$

where the parameters of these expression are reported in Table S1 and S2.

TABLE S2: Parameters of the potential energy surfaces reported in Eqs. (S7), (S8), and (S9). The following values are reported in atomic units.

Parameter	α	β	γ
k_0	0.411857	0.600329	0.601803
k_1	-0.086191	-0.031984	-0.031845
k_2	0.030146	0.002958	0.002974
k_3	-0.508824	-0.533005	-0.534277
k_4	0.899629	1.181328	1.183753
k_5	-0.494307	-0.516508	-0.517698
k_6	0.116953	0.136428	0.136926
k_7	0.003750	0.005385	0.005381

I.III. Kinetic energy operator

The kinetic energy operator $\hat{T}$ in the internal coordinates R and φ is set up according to the Wilson G-matrix formalism [3]

$$\hat{T} \simeq -\frac{\hbar^2}{2} \sum_{\mathrm{o}=1}^{2} \sum_{\mathrm{p}=1}^{2} \frac{\partial}{\partial q_{\mathrm{o}}} \left[G_{\mathrm{o,p}} \frac{\partial}{\partial q_{\mathrm{p}}} \right] , \tag{S10}$$

where p and o run over φ and R. The G-matrix elements $G_{\mathrm{o,p}}$ are computed via their inverse by numerical differentiation employing the central difference method

$$\left(G^{-1}\right)_{\mathrm{o,p}} = \sum_{i}^{3N} m_i \frac{\partial x_i}{\partial q_{\mathrm{o}}} \frac{\partial x_i}{\partial q_{\mathrm{p}}} , \tag{S11}$$

with atomic coordinates in the Cartesian frame $\boldsymbol{x}_i$ and $\boldsymbol{x}_j$ and m_i atomic mass.
In particular, for the two internal degrees of freedom considered in this work the G-matrix is diagonal and characterized by a constant G_{RR} element that equals 5.45×10^{-5} a.u. and by a nearly constant $G_{\varphi\varphi}$ that equals 2.40×10^{-4} a.u. These values match fairly well with the reciprocal of their normal mode reduced masses.

II. WAVE-PACKET PROPAGATION

The QD of the system is simulated through the QDng code [4] by numerical solution of the time-dependent Schrödinger equation on a spatial grid of 600 points on the C−I stretching and of 201 points on the H−C−I bending. In particular, the C−I stretching varies from 1.5 to 12 Å while the H−C−I bending is sampled between $\pm\pi$. Periodic boundary conditions are used to model the periodic behavior of the bending coordinate.
The wave function of the system is expanded in the diabatic basis as follows:

$$|\psi(t,R,\varphi)\rangle = \sum_{i} |\phi_i\rangle |\chi_i(t,R,\varphi)\rangle , \tag{S12}$$

where i runs over the excited electronic states included in the model and $|\chi(t,R,\varphi)\rangle$ is the nuclear WP evolving on the diabatic state $|\phi\rangle$. The initial condition of the QD (i.e., the WP at time zero) is set to the lowest vibrational eigenfunction of the ground state. In particular, in the vicinity of the minimum this can be well approximated by a harmonic potential, allowing to find the initial WP analytically. The vibrational frequencies and the reduced mass of the two modes were obtained at the MP2/ANO-R2 level of theory and they are reported in Table S3.
The WP propagation after impulsive excitation on the $^3Q_0$ state is performed via the Chebychev [5] scheme employing a time step of 1 a.u. (approximately 0.024 fs). A *right-pass* Butterworth filter is applied on both $^3Q_0$ and $^1Q_1$ at R=11.8 Å in order to absorb the WP that approaches the end of the grid. The wave function is re-normalized after each application of the filter.

TABLE S3: MP2/ANO-R2 vibrational frequencies and reduced masses of the C−I stretching (R) and H−C−I bending (φ) modes of CH_3I. The values match fairly well with those reported in Ref. [2] given in brackets.

Mode	Frequency (cm^{-1})	Reduced mass (amu[a])
R	569 (528[b])	5.03107
φ	883 (883[b])	1.14504

[a] atomic mass units
[b] experimental values from Ref. [2]

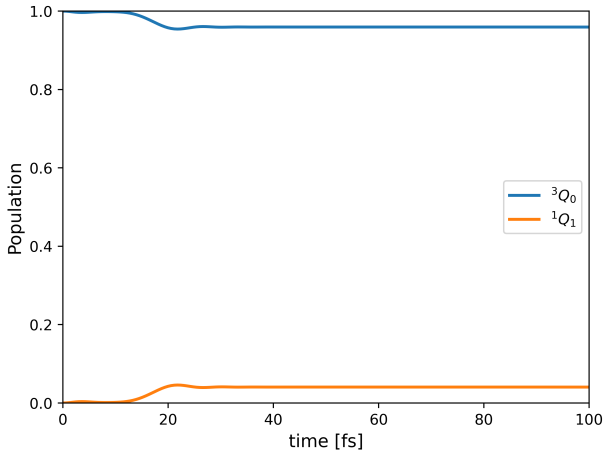

FIG. S2: Population dynamics of $^3Q_0$ (blue) and $^1Q_1$ (orange) states as predicted by explicit WP propagation.

The population dynamics predicted by such a setup is shown in Fig. S2

Electronic coherence can be defined as the off-diagonal element of the system density matrix $\varrho(t)$ defined as:

$$\varrho(t) = |\psi(t,R,\varphi)\rangle \langle\psi(t,R,\varphi)| \tag{S13}$$

Therefore, the $^3Q_0/^1Q_1$ coherence [$\varrho_{^3Q_0/^1Q_1}(t)$] can be directly linked to the overlap between the $^3Q_0$ and $^1Q_1$ WPs:

$$\varrho_{^3Q_0/^1Q_1}(t) = \left\langle \chi_{^3Q_0}(t,R,\varphi) \middle| \chi_{^1Q_1}(t,R,\varphi) \right\rangle \ , \tag{S14}$$

which in coordinate-space reads:

$$\varrho_{^3Q_0/^1Q_1}(t) = \int\int \chi^*_{^3Q_0}(t,R,\varphi)\chi_{^1Q_1}(t,R,\varphi)\, dR\, d\varphi \ . \tag{S15}$$

This equation represent a minimal basis to understand the key aspects behind coherence and decoherence dynamics in molecular systems. Relying on a semiclassical description of system-bath dynamics Fiete and Heller [6] identified three main sources of decoherence, namely: (i) displacement of the system WP, (ii) decay of the bath overlap, and (iii) phase jitter. The same mechanisms where then interpreted in the context of coupled electron-nuclear dynamics in molecules by Vacher *et al.* [7] as: (i) change in the electronic state population, (ii) change in the WP overlap, and (iii) dephasing of different WP components. The dependence of eq. S15 upon the electronic state population ($\varrho_i(t)$) can be made more explicit by introducing the normalized WPs $\bar{\chi}_i(t,R,\varphi)$ defined so that:

$$\chi_i(t,R,\varphi) = \left(\int\int \chi^*_i(t,R,\varphi)\chi_i(t,R,\varphi)\, dR\, d\varphi \right)^{1/2} \bar{\chi}_i(t,R,\varphi) = \sqrt{\varrho_i(t)}\, \bar{\chi}_i(t,R,\varphi) \ , \tag{S16}$$

which give rise to the following reformulation of Eq. (S15):

$$\varrho_{^3Q_0/^1Q_1}(t) = \sqrt{\varrho_{^3Q_0}(t)\varrho_{^1Q_1}(t)} \int\int \bar{\chi}^*_{^3Q_0}(t,R,\varphi)\bar{\chi}_{^1Q_1}(t,R,\varphi)\, dR\, d\varphi \ , \tag{S17}$$

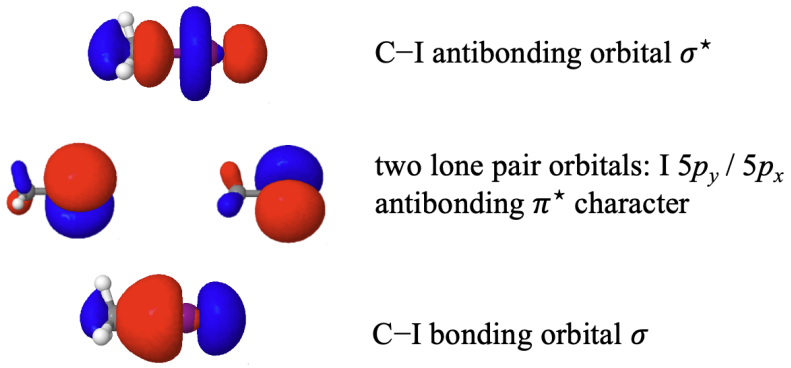

FIG. S3: Natural valence molecular orbitals $5p_x$, $5p_y$, σ and σ^* included in our MRCI calculations. The natural orbitals are here shown as isosurfaces (± 0.02 au).

which can be further simplified by noticing that in our model $\varrho_{^1Q_1}(t) = 1 - \varrho_{^3Q_0}(t)$ since $^3Q_0$ and $^1Q_1$ are the only two states connected via non-adiabatic coupling [see Eq. (S1)]:

$$\varrho_{^3Q_0/^1Q_1}(t) = \sqrt{\varrho_{^3Q_0}(t)[1-\varrho_{^3Q_0}(t)]} \int\int \bar{\chi}^*_{^3Q_0}(t,R,\varphi)\bar{\chi}_{^1Q_1}(t,R,\varphi)\, dR\, d\varphi \ . \tag{S18}$$

Eq. (18) shows a maximum for $\varrho_{^3Q_0}(t) = \varrho_{^1Q_1}(t) = 0.5$ as expected. In CH_3I our QD scheme predicts a relatively low $^3Q_0/^1Q_1$ branching ratio of 0.96:0.04, which gives a coherence prefactor ($\sqrt{\varrho_{^3Q_0}(t)\varrho_{^1Q_1}(t)}$) of roughly 0.20, corresponding already to the 39% of the maximum possible coherence magnitude, which is 0.5. However, this number can be slightly increased when considering larger alkyl iodides where the $^3Q_0/^1Q_1$ branching ratio is closer to the optimal 0.5:0.5 ratio [8].
The remaining mechanisms (ii) and (iii), neglected so far, are encoded in the overlap integral between the two normalized WPs in Eq. (S17). The time evolution of this factor is not trivial. However, in the case of CI dynamics, the magnitude of the WP overlap can be estimated qualitatively by invoking symmetry considerations. In particular, if the two electronic states intersecting at the CI have different symmetries, the integral of Eq. (S17) is vanishingly small. As discussed in the main text, this is the case for the CI dynamics in CH_3I, where the $^3Q_0$ and $^1Q_1$ states belong to the A_1 and $E(A')$ irreducible representation of the C_{3v} point group, respectively. Interestingly, in larger alkyl iodides such a restriction can in principle be removed by adjusting the substituent of the alkyl fragments to break the molecular symmetry.

III. ELECTRONIC STRUCTURE THEORY

Wave-function-based quantum chemistry (QC) calculations were performed on a CH_3I gas molecule with the MOLPRO package [9]. For the I^+ ion, we used all-electron triple-zeta Douglas-Kroll basis sets with diffuse functions and weighted core-valence sets (aug-cc-pwCVTZ-DK3) [10] to capture core-valence correlation effects. For the C atoms, all-electron double-zeta Douglas-Kroll basis sets with diffuse functions (aug-cc-pVDZ-DK) [11] were used. For the three H atoms, ANO-DK3 [12] basis sets were applied. We first optimized the ground state geometry of the CH_3I molecule with the multi-reference configuration interaction (MRCI) [13, 14] method. For the complete active space self-consistent field (CASSCF) [15] calculations, we used an active space of six electrons and four orbitals including two nearly degenerate lone pairs ($5p_x$ and $5p_y$ orbitals of I^+ ion) with slightly antibonding π^* character and C–I bonding σ and antibonding σ^* orbitals, as shown in Fig. S3. The self-consistent-field (SCF) optimization was carried out for an average of ten singlet states associated with this manifold. In the subsequent MRCI computation for the geometry optimization of the ground state, the I $4s$, $4p$, $4d$ shells and all C shells were correlated. The corresponding optimized XYZ coordinates are given in Table S4.
The valence-excited states were computed with the same active space of six electrons and four orbitals ($5p_x$, $5p_y$, σ and σ^*). The SCF optimization was carried out for an average of six triplet and ten singlet spin-free states associated with this manifold. On top of the CASSCF reference, the MRCI expansion additionally includes single and double excitations from the I $4s$, $4p$, $4d$ shells and all C shells. All these valence-excited triplet and singlet states entered the

TABLE S4: XYZ coordinates (in Å) for the optimized molecular structure of CH_3I in its ground electronic state.

atoms	X	Y	Z
C	0.0000	0.0000	−1.8010
I	0.0000	0.0000	0.3329
H	0.0000	1.0309	−2.1407
H	0.8927	−0.5154	−2.1407
H	−0.8927	−0.5154	−2.1407

spin-orbit calculations at the MRCI level. Spin-orbit (SO) effects were accounted for by diagonalizing the Breit-Pauli SO matrix in the basis of correlated scalar-relativistic states [16]. For the core-excited $4d^{-1}$ states, the CASSCF treatment was performed in terms of sixteen electrons and nine orbitals including five $4d$ orbitals and four valence orbitals ($5p_x$, $5p_y$, σ and σ^*). The SCF optimization was carried out for an average of 26 triplet and 30 singlet states. On top of the CASSCF reference, in order to exclude the valence-excited states, appropriate changes were further employed in the subsequent MRCI treatment such that the I $4d$ orbitals have at most nine $4d$ electrons for internal and semi-internal substitutions, giving rise to 20 triplet and 20 singlet core-excited spin-free states. All these core-excited states entered the spin-orbit calculations. The MRCI transition dipole matrix elements between wave functions for these valence- and core-excited states were derived according to the procedure described in Ref. [17].
We first computed the potential energy surfaces (PES) of CH_3I along the C−I distance coordinate as indicated in Fig. S4(b) while the remaining nuclear degrees of freedom are kept frozen. The conical intersection between the $^1Q_1$ and $^3Q_0$ excited states is located at a C−I distance of around 2.4 Å as shown in Fig. S4(a). For the two-dimensional model in our work, we additionally considered the H−C−I bending, which acts as the coupling mode to the $^1Q_1$ and $^3Q_0$ states. In particular, we define the change of angle $\Delta\varphi$ between H_1 and the CH_3 main rotational axes. In this frame, the H−C−I bending motion occurs exclusively within the H_1−C−I plane as illustrated in Fig. S4(c). To obtained the two dimensional scan, we chose the distance of the C−I bond from 1.60 Å to 4.00 Å with a step size of 0.20 Å; for each C−I distance, we scan $\Delta\varphi$ from −40° to 40° with a step size of 10°.

IV. DERIVATION OF THE HD-FWM SIGNAL

The electric field ($\mathbf{E}$) emitted in the direction $\boldsymbol{k}$ at the time t by the FWM interaction can be traced back to the third order non-linear polarization $\mathbf{P}^{(3)}(t)$ according to

$$\mathbf{E}_{\boldsymbol{k},\mathrm{FWM}}(t) \propto -i\mathbf{P}^{(3)}(t) \ , \tag{S19}$$

which is evaluated via perturbation theory as discussed in Ref. [18]

$$\mathbf{P}^{(3)}(\boldsymbol{k},t) \propto -i\int\int\int dt_1 dt_2 dt_3 \mathbf{E}(t-t_3)\mathbf{E}(t-t_2-t_3)\mathbf{E}(t-t_1-t_2-t_3)R^{(3)}(t_1,t_2,t_3) \quad , \tag{S20}$$

where $R^{(3)}$ is the third-order response function and $\mathbf{E}(t)$ is the electric field that generates the FWM response. In particular, we distinguish between the electric field that drives FWM_1 [called $\mathbf{E}_1(t)$] and the electric field that induces FWM_2 [$\mathbf{E}_2(t)$]:

$$\begin{aligned}\mathbf{E}_1(t) = &\hat{\boldsymbol{e}}_{\mathrm{XUV}}\mathrm{E}_{\mathrm{XUV}}(t)\exp(i\boldsymbol{k}_{\mathrm{XUV}}\cdot\boldsymbol{r} - i\omega_{\mathrm{XUV}}t) + \\ &+ \hat{\boldsymbol{e}}_{\mathrm{NIR}_1}\mathrm{E}_{\mathrm{NIR}_1}(t)\exp(i\boldsymbol{k}_{\mathrm{NIR}_1}\cdot\boldsymbol{r} - i\omega_{\mathrm{NIR}_1}t) + \\ &+ \hat{\boldsymbol{e}}_{\mathrm{NIR}_2}\mathrm{E}_{\mathrm{NIR}_2}(t)\exp(i\boldsymbol{k}_{\mathrm{NIR}_2}\cdot\boldsymbol{r} - i\omega_{\mathrm{NIR}_2}t)\end{aligned} \tag{S21}$$

$$\begin{aligned}\mathbf{E}_2(t) = &\hat{\boldsymbol{e}}_{\mathrm{XUV}}\mathrm{E}_{\mathrm{XUV}}(t)\exp(i\boldsymbol{k}_{\mathrm{XUV}}\cdot\boldsymbol{r} - i\omega_{\mathrm{XUV}}t) + \\ &+ \hat{\boldsymbol{e}}_{\mathrm{NIR}_1}\mathrm{E}_{\mathrm{NIR}_1}(t)\exp(i\boldsymbol{k}_{\mathrm{NIR}_1}\cdot\boldsymbol{r} - i\omega_{\mathrm{NIR}_1}t) + \\ &+ \hat{\boldsymbol{e}}_{\mathrm{VIS}}\mathrm{E}_{\mathrm{VIS}}(t)\exp(i\boldsymbol{k}_{\mathrm{VIS}}\cdot\boldsymbol{r} - i\omega_{\mathrm{VIS}}t + i\Delta\gamma)\end{aligned} \tag{S22}$$

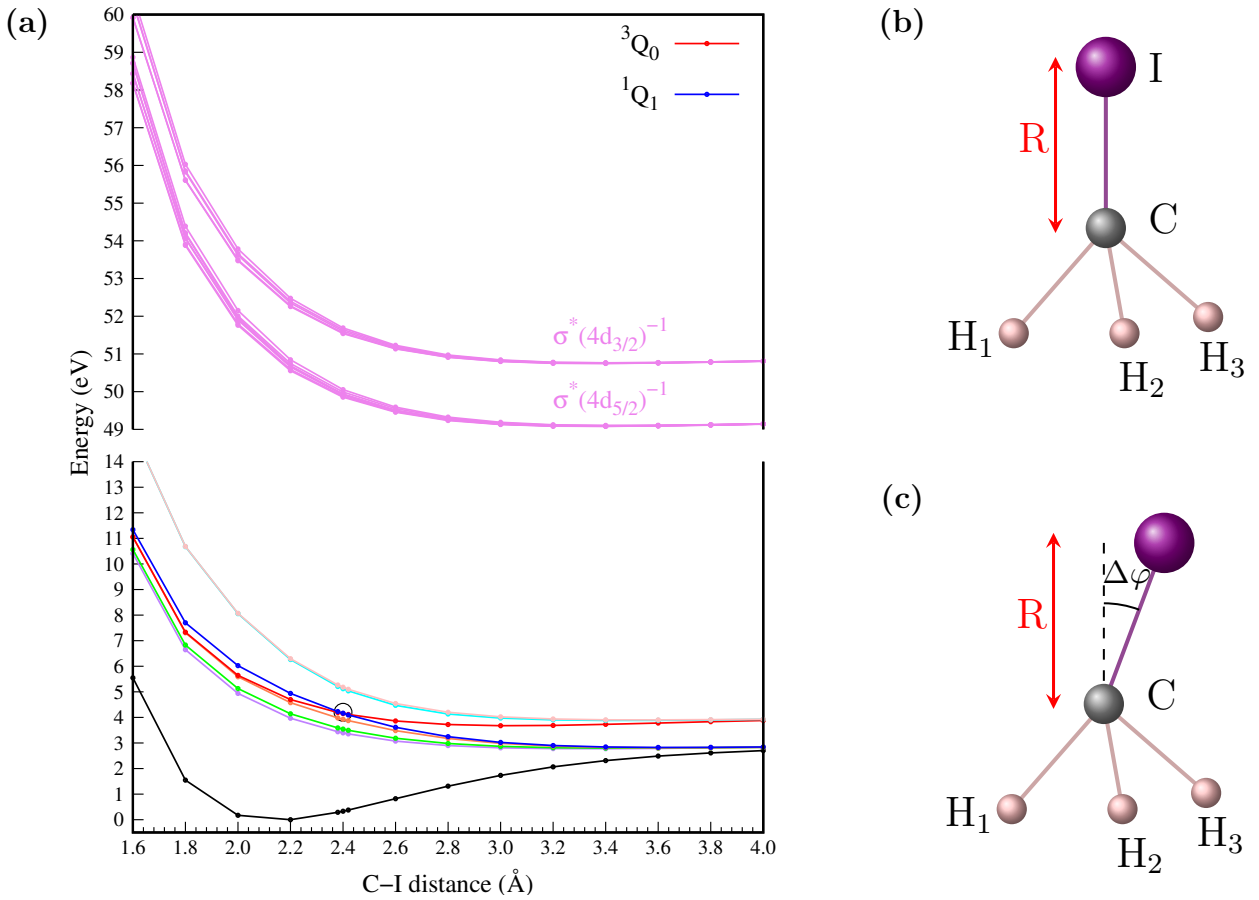

FIG. S4: (a) The PESs of the ground and the excited states of CH_3I along the C−I bond distance. The conical intersection between the $^1Q_1$ and $^3Q_0$ excited states is indicated by the black circle. (b-c) Definition of the nuclear degrees of freedom spanning the effective Hamiltonian defined in Eq. (S1): (b) the C−I bond distance R; (c) the change of H−C−I bending angle $\Delta\varphi$.

with $\hat{\boldsymbol{e}}$ the polarization of the i electric field components with corresponding envelope $\mathrm{E}_i(t)$. $\Delta\gamma$ is the phase offset between the NIR_2 and the VIS pulse. Further in the manuscript we will show how cycling this parameter enables to retrieve the complex response function of the system.

The noncollinear geometry of our experiment allows to isolate the polarization component emitted in the $\boldsymbol{k}_s = \boldsymbol{k}_1 + \boldsymbol{k}_2 - \boldsymbol{k}_3$ phase-matching direction where $\boldsymbol{k}_1$ and $\boldsymbol{k}_2$ always correspond to the XUV and NIR_1 wave vectors, while $\boldsymbol{k}_3$ can be either associated with NIR_2 or VIS. Inserting these two equations into Eq. (S20) and neglecting highly oscillating terms (i.e. imposing rotating wave approximation; RWA) we get:

$$\mathbf{P}_1^{(3)}(\boldsymbol{k}_s,t) \propto -i\int\int\int dt_1dt_2dt_3 E_{\mathrm{NIR}_2}(t-t_3)E_{\mathrm{NIR}_1}(t-t_2-t_3)E_{\mathrm{XUV}}(t-t_1-t_2-t_3)\times \\ \times\, e^{i(\omega_{\mathrm{XUV}}+\omega_{\mathrm{NIR}_1}-\omega_{\mathrm{NIR}_2})t_3}e^{i(\omega_{\mathrm{XUV}}+\omega_{\mathrm{NIR}})t_2}e^{i\omega_{\mathrm{XUV}}t_1}R_1^{(3)}(t_1,t_2,t_3) \tag{S23}$$

$$\mathbf{P}_2^{(3)}(\boldsymbol{k}_s,t) \propto -i\int\int\int dt_1dt_2dt_3 E_{\mathrm{VIS}}(t-t_3)E_{\mathrm{NIR}_1}(t-t_2-t_3)E_{\mathrm{XUV}}(t-t_1-t_2-t_3)\times \\ \times\, e^{i(\omega_{\mathrm{XUV}}+\omega_{\mathrm{NIR}_1}-\omega_{\mathrm{VIS}})t_3}e^{i(\omega_{\mathrm{XUV}}+\omega_{\mathrm{NIR}_1})t_2}e^{i\omega_{\mathrm{XUV}}t_1}R_2^{(3)}(t_1,t_2,t_3)\,e^{i\Delta\gamma} \tag{S24}$$

Here, the relative intensity between E_{NIR_2} and E_{VIS} can be chosen such that $\mathbf{P}_1^{(3)} >> \mathbf{P}_2^{(3)}$. Doing so, the electric field emitted by $\mathbf{P}_1^{(3)}$ can be used as a local oscillator (LO) for the one emitted by $\mathbf{P}_2^{(3)}$ (which can be called *signal* in the standard *heterodyne*-detection nomenclature). As a first approximation, we impose the *impulsive* limit assuming

infinitely short laser pulses. This corresponds to the limit of perfect time resolution. The impact of finite pulse duration on the signal is then recovered by convoluting the signal with the instrumental response function as discussed in Sec. V. Under this approximation the third order polarization is equal to the system response function. Eqs. (S23) and (S24) can be further simplified noticing that the three pulses are overlapped in time (i.e. $t_1 = t_2 = 0$):

$$\mathbf{P}^{(3)}_{\mathrm{LO}}(\boldsymbol{k}_s, t_3; T) \propto -iR^{(3)}_{\mathrm{LO}}(t_3; T) \tag{S25}$$

$$\mathbf{P}^{(3)}_{\mathrm{S}}(\boldsymbol{k}_s, t_3; T) \propto -iR^{(3)}_{\mathrm{S}}(t_3; T)\, e^{i\Delta\gamma} \tag{S26}$$

where we have also introduced the *heterodyne*-detection nomenclature. Moreover, in our experiment the FWM process is driven after a time delay T with respect to the initial *actinic* UV pump pulse. For this reason, we also introduce the parametric dependence over this time delay.

IVa. Spectral interference

After being emitted from the sample the FWM field is diffracted by a reflective grating, which corresponds to a Fourier transform of the signal and LO electric fields i.e:

$$\mathbf{E}^{(3)}_{\mathrm{LO}}(\boldsymbol{k}_s, \Omega; T) \propto \int_0^{+\infty} R^{(3)}_{\mathrm{LO}}(t_3; T)\, e^{i\Omega t_3}\, dt_3 \tag{S27}$$

$$\mathbf{E}^{(3)}_{\mathrm{S}}(\boldsymbol{k}_s, \Omega; T) \propto e^{i\Delta\gamma} \int_0^{+\infty} R^{(3)}_{\mathrm{S}}(t_3; T)\, e^{i\Omega t_3}\, dt_3 \ . \tag{S28}$$

After the grating the signal is measured by a square-law detector (CCD camera). Here the total signal $[\mathrm{I}_{\mathrm{T}}(\boldsymbol{k}_s, \Omega; T)]$ measured by the CCD camera reads:

$$\begin{aligned}\mathrm{I}_{\mathrm{T}}(\boldsymbol{k}_s, \Omega; T) \propto \int dt \Big[&\mathbf{E}^{(3)}_{\mathrm{LO}}(\boldsymbol{k}_s, \Omega; T)e^{-i\Omega t} + \mathbf{E}^{(3)}_{\mathrm{LO}}(\boldsymbol{k}_s, -\Omega; T)e^{i\Omega t} + \\ &+ \mathbf{E}^{(3)}_{\mathrm{S}}(\boldsymbol{k}_s, \Omega; T)e^{-i\Omega t} + \mathbf{E}^{(3)}_{\mathrm{S}}(\boldsymbol{k}_s, -\Omega; T)e^{i\Omega t} \Big]^2 \ .\end{aligned} \tag{S29}$$

After taking the square and neglecting highly oscillating terms, the interference (i.e., the heterodyne detected-$\mathrm{Hd}^{(3)}$ signal) between the signal and the LO reads:

$$\mathrm{Hd}^{(3)}(\boldsymbol{k}_s, \Omega; T) \propto 2\mathrm{Re}\left[\mathbf{E}^{(3)}_{\mathrm{LO}}(\boldsymbol{k}_s, -\Omega; T)\mathbf{E}^{(3)}_{\mathrm{S}}(\boldsymbol{k}_s, \Omega; T)\right] \quad . \tag{S30}$$

This equation defines the final target of our simulations—the measurement observable—and it is here evaluated by combining Eq. (S27) and Eq. (S28).

IVb. Evaluating the Signal and LO response functions

Signal and LO fields are evaluated by expanding their response function as combination of Feynman diagrams, each one corresponding to a specific quantum pathway of Fig. S5. In particular, we obtain:

$$R^{(3)}_{\mathrm{LO}}(t_3; T) = \sum_{\alpha\in\{a,\ldots,h\}} R^{(3),\alpha}_{\mathrm{LO}}(t_3; T) \tag{S31}$$

$$R^{(3)}_{\mathrm{S}}(t_3; T) = \sum_{\beta\in\{i,\ldots,l\}} R^{(3),\beta}_{\mathrm{S}}(t_3; T) \ , \tag{S32}$$

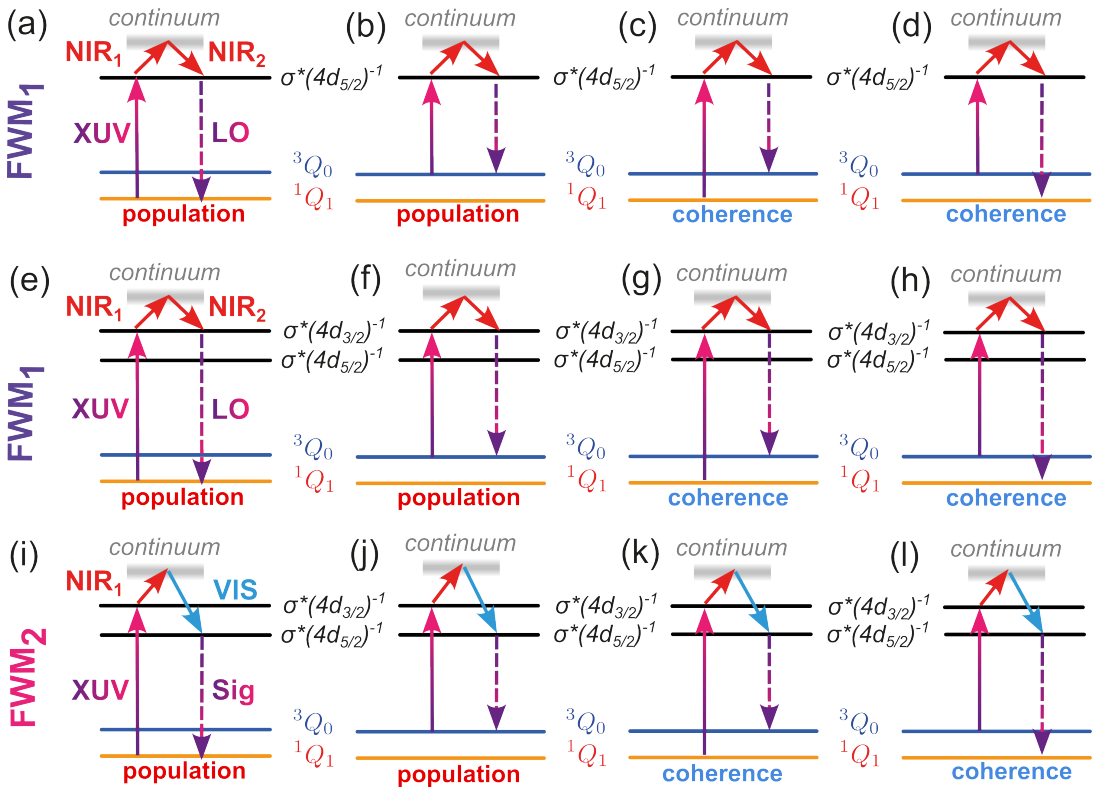

FIG. S5: Diagrams of quantum pathways contributing to FWM_1 and FWM_2 in the $\boldsymbol{k}_s = \boldsymbol{k}_1 + \boldsymbol{k}_2 - \boldsymbol{k}_3$ phase matching direction.

where the indices α and β encode the different diagrams of Fig. S5. Interestingly, invoking spectral overlap and transition dipole moment considerations allows to drastically reduce the number of pathways to be considered in the simulation, thereby reducing its computational cost. In particular, we note that the emission from the $\sigma^*(4d_{5/2})^{-1}$ core excited state towards the valence manifold is energetically well separated from the corresponding emission of the $\sigma^*(4d_{3/2})^{-1}$ state. Therefore, quantum pathways of FWM_1 that emit from $\sigma^*(4d_{3/2})^{-1}$ will not overlap spectrally with FWM_2 and hence do not contribute to the Hd-FWM signal. This allows to limit the potentially relevant pathways of FWM_1 to the diagrams (a) to (d) of Fig. S5. Moreover, we note that the $\sigma^*(4d_{5/2})^{-1} \rightarrow {}^3Q_0$ and ${}^1Q_1 \rightarrow \sigma^*(4d_{3/2})^{-1}$ transitions are characterized by vanishingly small transition dipole moments thereby reducing the relevant quantum pathways to the diagrams (a) for FWM_1 and (l) for FWM_2. These diagrams correspond to the signal (l) and LO (a) pathways discussed in the main manuscript. The Sig and LO response functions can be thus evaluated as:

$$R_{\mathrm{LO}}^{(3),a}(t_3;T) \propto \left\langle \chi^1Q_1(T)\right| e^{i\hat{H}t_3}\hat{\boldsymbol{\mu}}^1Q_1,\sigma^*(4d_{5/2})^{-1}\hat{\boldsymbol{\alpha}}_{\mathrm{N/N}}e^{-i\hat{H}t_3}\hat{\boldsymbol{\mu}}^1Q_1,\sigma^*(4d_{5/2})^{-1}\left|\chi^1Q_1(T)\right\rangle \tag{S33}$$

$$R_{\mathrm{S}}^{(3),l}(t_3;T) \propto \left\langle \chi^1Q_1(T)\right| e^{i\hat{H}t_3}\hat{\boldsymbol{\mu}}^1Q_1,\sigma^*(4d_{5/2})^{-1}\hat{\boldsymbol{\alpha}}_{\mathrm{N/V}}e^{-i\hat{H}t_3}\hat{\boldsymbol{\mu}}^3Q_0,\sigma^*(4d_{3/2})^{-1}\left|\chi^3Q_0(T)\right\rangle \ , \tag{S34}$$

where $\hat{\boldsymbol{\alpha}}_{\mathrm{N/N}}$ and $\hat{\boldsymbol{\alpha}}_{\mathrm{N/V}}$ are the transition polarizability of the off-resonant Raman processes driven by the $\mathrm{NIR}_1/\mathrm{NIR}_2$ and by the $\mathrm{NIR}_1/\mathrm{VIS}$ pulses, respectively. Under the perturbative limit, the Raman polarizability for a transition between two quantum states e and e' driven by the superposition of two distinct electric fields with envelopes $\mathrm{E}_1(\omega)$ and $\mathrm{E}_2(\omega)$ and carrier frequencies ω_1 and ω_2 reads:

$$\boldsymbol{\alpha}_{e\rightarrow e'} = \sum_k \hat{\boldsymbol{\mu}}_{ek}\hat{\boldsymbol{\mu}}_{ke'}\int \frac{d\omega}{2\pi}\frac{\mathrm{E}_1(\omega)\mathrm{E}_2^*(\omega+\Delta-\omega_{ee'})}{\omega+\omega_1-\omega_{ek}+i\epsilon} \ , \tag{S35}$$

where $\omega_{ee'}$ is the $e \rightarrow e'$ excitation energy, Δ is the $\mathrm{E}_1/\mathrm{E}_2$ detuning, i.e. $\omega_1 - \omega_2$, and ϵ is a positive infinitesimal electronic dephasing term. Here the index k formally runs over all the eigenstates of the system Hamiltonian. However, E_1 and E_2 pulses are usually characterized by finite bandwidth thus limiting the number of states to be included in

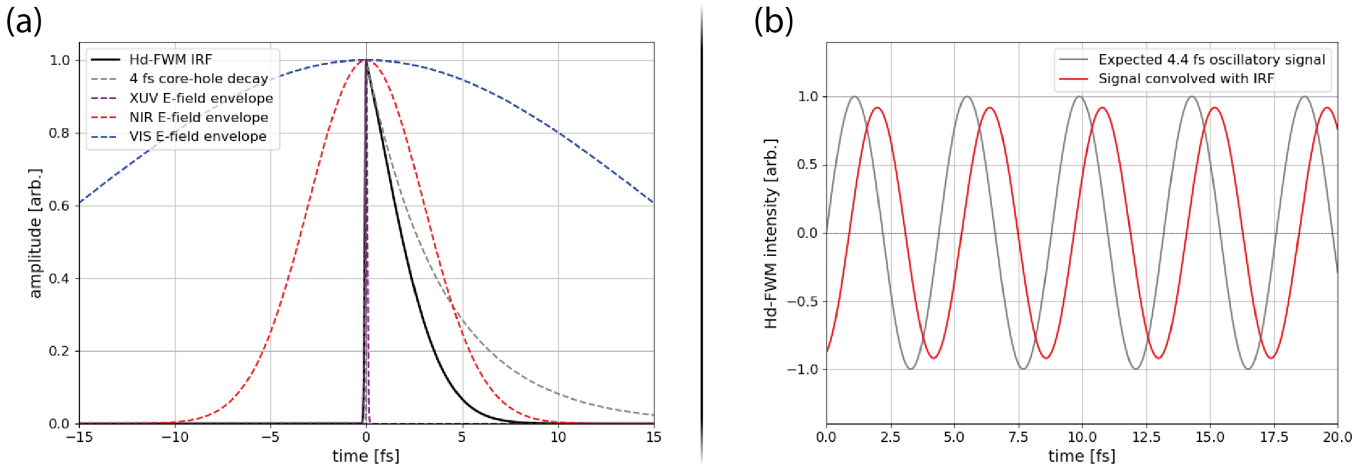

FIG. S6: Anticipated temporal resolution of the Hd-FWM scheme applied to the photodynamics of CH_3I. (a) Electric-field envelopes (dashed lines), iodine $4d^{-1}$ core-hole decay (gray solid line), and resulting Hd-FWM IRF (black solid line). The IRF is gated on its rising edge by the XUV field envelope. (b) Applying the IRF function from (a) to an anticipated 4.4 fs oscillating Hd-FWM signal (gray) results is a slightly phase-shifted but well resolved measurable signal (red). The phase shift is due to the IRF being asymmetric in time.

this expression. In the case of $\boldsymbol{\alpha}_{\mathrm{N/N}}$ the detuning term Δ is zero, therefore, in order to prevent any population transfer from a core excited state to another, the NIR bandwidth must be smaller than the $\sigma^*(4d_{3/2})^{-1}$ - $\sigma^*(4d_{5/2})^{-1}$ energy gap (approximately 1.7 eV). Under this approximation Eq. (S35) becomes:

$$\boldsymbol{\alpha}_{\mathrm{N/N}} = \sum_k |\hat{\boldsymbol{\mu}}_{\sigma^*(4d_{5/2})^{-1}k}|^2 \int \frac{d\omega}{2\pi} \frac{\mathrm{E}_{\mathrm{NIR}_1}(\omega)\mathrm{E}_{\mathrm{NIR}_2}(\omega)}{\omega + \omega_{\mathrm{NIR}_1} - \omega_{\sigma^*(4d_{5/2})^{-1}k} + i\epsilon} \,, \tag{S36}$$

where we have assumed a real valued envelope for both NIR pulses. Conversely, in the case of $\boldsymbol{\alpha}_{\mathrm{N/V}}$ the detuning between the VIS and NIR_1 pulses is large enough to selectively promote the $\sigma^*(4d_{3/2})^{-1}$ transfer to $\sigma^*(4d_{5/2})^{-1}$. Therefore the transition polarizability becomes:

$$\boldsymbol{\alpha}_{\mathrm{N/V}} = \sum_k \hat{\boldsymbol{\mu}}_{\sigma^*(4d_{3/2})^{-1}k}\hat{\boldsymbol{\mu}}_{k\sigma^*(4d_{5/2})^{-1}} \int \frac{d\omega}{2\pi} \frac{\mathrm{E}_{\mathrm{NIR}_1}(\omega)\mathrm{E}_{\mathrm{VIS}}(\omega + \Delta - \omega_{\sigma^*(4d_{3/2})^{-1}\sigma^*(4d_{5/2})^{-1}})}{\omega + \omega_{\mathrm{NIR}_1} - \omega_{\sigma^*(4d_{3/2})^{-1}k} + i\epsilon} \,. \tag{S37}$$

V. HETERODYNED FOUR-WAVE-MIXING TEMPORAL INSTRUMENT RESPONSE FUNCTION

For resolving the fastest 4.4 fs oscillatory features in the simulated Hd-FWM trace (see Fig. 3 of the main manuscript), one has to calculate the instrument response function (IRF) out of temporal overlap with the actinic UV pulse as these oscillatory features occur in the atomic limit (long time delays). Realistic laser-pulse durations are considered for calculating the IRF: $\tau_{NIR} = 5\,\mathrm{fs}$, $\tau_{VIS} = 25\,\mathrm{fs}$, and $\tau_{XUV} = 100\,\mathrm{as}$ for the isolated attosecond XUV pulse. Fig. S6(a) depicts the respective electric field envelopes of these pulses, as well as the iodine $4\mathrm{d}^{-1}$ core-hole lifetime of 4 fs [19, 20] and the IRF resulting from the $\chi^{(3)}$ FWM process (black solid line). A necessary requirement for the Hd-FWM process is the core-level iodine 4d→5p transition, which is only triggered by XUV photons. Hence, the leading edge of the IRF follows the field-envelope of the attosecond XUV pulse. Even though the tail of the IRF is dominated by the NIR/VIS pulse durations convolved with the core-hole lifetime, the decisive factor for the achievable temporal resolution is the steep XUV-gated rising amplitude [see Fig. S6(a)]. This results in a sub-femtosecond resolution while the longer IRF tail just leads to an overall phase-shift of the signal trace as depicted in Fig. S6(b). In other words, the combination of XUV, NIR and VIS pulses acts similarly to a hybrid coherent anti-Stokes Raman spectroscopy (CARS) pulse scheme, where the high temporal resolution is guaranteed by the attosecond XUV pulse while the precise energy resolution (i.e. selection of specific quantum pathways) is provided by the few-tens of fs optical pulses. Besides the pulse durations themselves, the time-delay stability between the pulses influences the ultimately achievable temporal resolution of the measurement. Recently, multiple schemes for an active stabilization of pulse delays to the sub-femtosecond level have been demonstrated [21–23]. Therefore,

we expect an overall achievable temporal inter-pulse stability to be on the sub-femtosecond level and hence to have no significant impact on the IRF.

VI. IMPACT OF LASER-PULSE NOISE ON THE HETERODYNED FOUR-WAVE-MIXING SIGNAL

In a real-world experiment, fluctuations in the laser-pulse parameters exist and thus such noise has to be considered for any anticipated potential Hd-FWM measurement signal. Commercial, state-of-the-art amplified kHz-repetition-rate femtosecond Titanium:Sapphire laser systems typically provide a power stability better than 0.5% [24], even down to 0.2% [25]. Advanced 400 nm-VIS-pulse generation schemes also stay way below the 0.5% threshold (e.g., 0.39% in [26]). In addition, CEP stabilization to better than 200 mrad (e.g., 144 mrad in [27]) is readily available. Hence, for testing the impact of realistic laser-pulse-induced noise, the QD simulation outlined in SM Sec. IV has been performed 200 times with added random noise of 0.5% in intensity and 200 mrad in CEP, sampled from the corresponding normal distribution. The resulting Hd-FWM signal is presented in Fig. S7. Even considering this laser-pulse noise, the Hd-FWM interference contrast is barely reduced, showing the robustness of the technique. This surprising robustness is a consequence of the heterodyned character of the experimental scheme, where only relative noise between the NIR_2 and the VIS pulses comes into play. The Hd-FWM signature still clearly exhibits the 4.4 fs oscillatory signatures in the atomic limit.

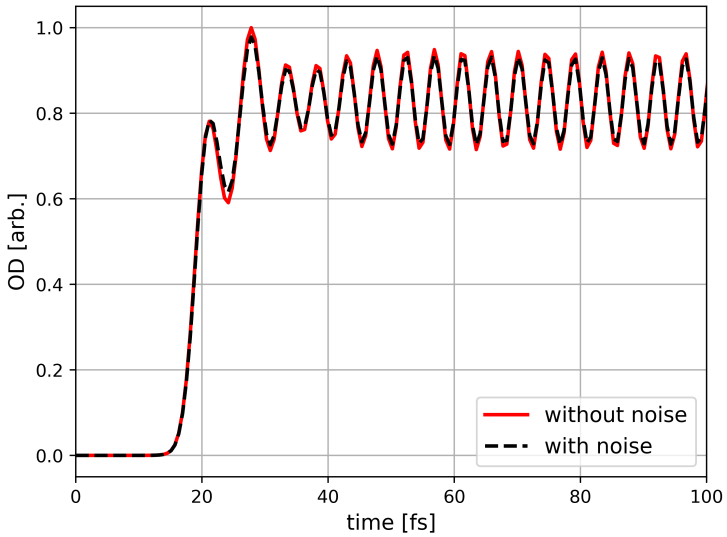

FIG. S7: Total FWM intensity as defined in Eq. (1) of the main manuscript. The red solid line highlights the total signal in the limit of perfect pulses without noise while the black dashed line depicts the FWM intensity when realistic laser noise is considered in the simulation. In particular, we account for shot-to-shot instability by averaging the total signal over 200 different pulse realizations obtained by sampling each individual pulse parameter from the corresponding normal distribution characterized by the expected standard deviation (i.e. 200 mrad for the CEP and 0.5% for pulse intensity).

* prupprecht@lbl.gov; These authors contributed equally to this work.
† francesco.montorsi4@unibo.it; These authors contributed equally to this work.
‡ dneumark@berkeley.edu
§ keeferd@mpip-mainz.mpg.de
¶ srl@berkeley.edu

[1] Y. Amatatsu, S. Yabushita, and K. Morokuma, Full nine-dimensional ab-initio potential energy surfaces and trajectory studies of A-band photodissociation dynamics: $CH_3I^* \rightarrow CH_3+I$, CH_3+I^*, and $CD_3I^* \rightarrow CD_3+I$, CD_3+I^*, J. Chem. Phys. **104**, 9783–9794 (1996).

[2] D. Xie, H. Guo, Y. Amatatsu, and R. Kosloff, Three-dimensional photodissociation dynamics of rotational state selected methyl iodide, J. Chem. Phys. A **104**, 1009–1019 (2000).

[3] P. H. Berens and K. R. Wilson, Molecular dynamics and spectra. I. Diatomic rotation and vibration, J. Chem. Phys. **74**, 4872–4882 (1981).

[4] M. Kowalewski and R. de Vivie-Riedle, Qdng: A grid based molecular quantum dynamics package, `https://doi.org/10.5281/zenodo.10944496`, Zenodo (2024).

[5] H. Tal-Ezer and R. Kosloff, An accurate and efficient scheme for propagating the time dependent Schrödinger equation, J. Chem. Phys. **81**, 3967–3971 (1984).

[6] G. A. Fiete and E. J. Heller, Semiclassical theory of coherence and decoherence, Phys. Rev. A **68**, 10.1103/physreva.68.022112 (2003).

[7] M. Vacher, M. J. Bearpark, M. A. Robb, and J. P. Malhado, Electron dynamics upon ionization of polyatomic molecules: Coupling to quantum nuclear motion and decoherence, Phys. Rev. Lett. **118**, 10.1103/physrevlett.118.083001 (2017).

[8] K. F. Chang, H. Wang, S. M. Poullain, J. González-Vázquez, L. Bañares, D. Prendergast, D. M. Neumark, and S. R. Leone, Conical intersection and coherent vibrational dynamics in alkyl iodides captured by attosecond transient absorption spectroscopy, J. Chem. Phys. **156** (2022).

[9] H. J. Werner, P. J. Knowles, G. Knizia, F. R. Manby, and M. Schütz, Molpro: A general-purpose quantum chemistry program package, Wiley Rev: Comp. Mol. Sci. **2**, 242 (2012).

[10] J. G. Hill and K. A. Peterson, Correlation consistent basis sets for explicitly correlated wavefunctions: Pseudopotential−based basis sets for the post−d main group elements Ga–Rn, J. Chem. Phys. **141**, 094106 (2014).

[11] T. H. Dunning Jr., Gaussian basis sets for use in correlated molecular calculations. I. The atoms boron through neon and hydrogen, J. Chem. Phys. **90**, 1007 (1989).

[12] P. O. Widmark, P. Å. Malmqvist, and B. O. Roos, Density matrix averaged atomic natural orbital (ANO) basis sets for correlated molecular wave functions I. First row atoms, Theoret. Chim. Acta **77**, 291 (1990).

[13] H. Werner and P. J. Knowles, An efficient internally contracted multiconfiguration—reference configuration interaction method, J. Chem. Phys. **89**, 5803 (1988).

[14] P. J. Knowles and H. J. Werner, Internally contracted multiconfiguration−reference configuration interaction calculations for excited states, Theoret. Chim. Acta **84**, 95 (1992).

[15] T. Helgaker, P. Jørgensen, and J. Olsen, *Molecular Electronic-Structure Theory* (Wiley, Chichester, 2000).

[16] A. Berning, M. Schweizer, H.-J. Werner, P. J. Knowles, and P. Palmieri, Spin-orbit matrix elements for internally contracted multireference configuration interaction wavefunctions, Mol. Phys. **98**, 1823 (2000).

[17] A. Mitrushchenkov and H.-J. Werner, Calculation of transition moments between internally contracted MRCI wave functions with non-orthogonal orbitals, Mol. Phys. **105**, 1239 (2007).

[18] S. Mukamel, *Principles of Nonlinear Optical Spectroscopy* (Oxford University Press, New York, 1995).

[19] L. Nahon, P. Morin, and F. C. Farnoux, Relaxation of the nd→(n+1)p resonances in atomic bromine and iodine, Phys. Scr. **1992**, 104 (1992).

[20] L. Drescher, M. Galbraith, G. Reitsma, J. Dura, N. Zhavoronkov, S. Patchkovskii, M. Vrakking, and J. Mikosch, Communication: XUV transient absorption spectroscopy of iodomethane and iodobenzene photodissociation, J. Chem. Phys. **145** (2016).

[21] M. Chini, H. Mashiko, H. Wang, S. Chen, C. Yun, S. Scott, S. Gilbertson, and Z. Chang, Delay control in attosecond pump-probe experiments, Opt. Express **17**, 21459 (2009).

[22] M. Huppert, I. Jordan, and H. J. Wörner, Attosecond beamline with actively stabilized and spatially separated beam paths, Rev. Sci. Instrum. **86** (2015).

[23] F. Schlaepfer, M. Volkov, N. Hartmann, A. Niedermayr, Z. Schumacher, L. Gallmann, and U. Keller, Phase stabilization of an attosecond beamline combining two IR colors, Opt. Express **27**, 22385 (2019).

[24] `https://www.coherent.com/content/dam/coherent/site/en/resources/datasheet/lasers/astrella-ds.pdf`, stability specifications of a typical state-of-the-art Titanium:Sapphire laser system (Coherent Inc. Astrella).

[25] P. D. Rupprecht, *Ultrafast Laser Control of Molecular Quantum Dynamics from a Core-Electron Perspective*, Ph.D. thesis, Ruperto-Carola-University of Heidelberg (2022).

[26] F. Hu, Z. Wang, Q. Yao, W. Cao, Q. Zhang, and P. Lu, Clean hundred-μJ-level sub-6-fs blue pulses generated with helium-assisted solid thin plates, Opt. Lett. **48**, 2555 (2023).

[27] M. Musheghyan, F. Lücking, Z. Cheng, H. Frei, and A. Assion, 0.24 TW ultrabroadband, CEP-stable multipass Ti:Sa amplifier, Opt. Lett. **44**, 1464 (2019).